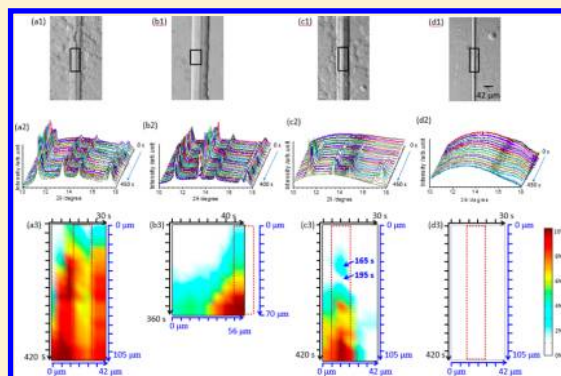


Flow-Induced Precursors of Isotactic Polypropylene: An *in Situ* Time and Space Resolved Study with Synchrotron Radiation Scanning X-ray Microdiffraction

Fengmei Su, Weiming Zhou, Xiangyang Li,* Youxin Ji, Kunpeng Cui, Zeming Qi, and Liangbin Li*

National Synchrotron Radiation Lab and College of Nuclear Science and Technology, CAS Key Laboratory of Soft Matter Chemistry, University of Science and Technology of China, Hefei, China

ABSTRACT: Shear-induced precursors obtained by fiber pulling with high shear rate in undercooled melts of isotactic polypropylene (iPP) at a wide temperature range were investigated by highly time and space resolved synchrotron radiation scanning X-ray microdiffraction (SR- μ SXRD). X-ray diffraction patterns in spot area of $4.9 \times 5.3 \mu\text{m}^2$ were obtained by scanning proximities around the fiber with step size of $7 \mu\text{m}$ immediately after shear and during the sequent crystallization process. The crystallinity derived from SR- μ SXRD indicates that the structure of precursors was determined by shear temperature, providing a high shear rate was imposed. At shear temperatures around or below the melting temperature, the presence of crystal diffraction immediately after shear indicates the formation of crystalline precursors with reduced density by increasing shear temperature. At shear temperatures in between melting and equilibrium melting temperature, the formation of noncrystalline precursors is supported by three evidence: (i) formation of shear-induced ordered structure indicated by preference of crystallization on fiber surface; (ii) absence of crystal signal immediately after shear; (iii) induction time necessary for transforming noncrystalline precursor into crystal. The experimental results suggest that the structure of noncrystalline precursors probably is aggregates of partially ordered chain segments which orient along the shear direction.



INTRODUCTION

Flow-induced crystallization (FIC) has attracted considerable attention because of its importance to polymer physics and industry. Complex flow field during processing such as extrusion, fiber spinning, film blowing, etc., dramatically influences the final morphology and properties of polymer products.^{1–7} Flow can increase the crystallization rate by orders of magnitude^{8–10} and can also change the crystalline morphology, which significantly increases stiffness and strength.^{11–17} Though great experimental and theoretical efforts have been dedicated to FIC in the past 70 years, discrepancies still exist on some fundamental issues such as the structures of shish/row nuclei^{18–25} or precursors^{26–32} and the roles of molecular weight^{33–38} and flow field parameters.^{39–44} As the final structure and properties strongly depend on the initial structure induced by flow, attention has been focused on the flow-induced nuclei or precursors in recent years, which is the essential flavor to construct the molecular mechanism of FIC.

Flow-induced precursors have been widely studied through different approaches on their structure, dynamics, and thermal stability, where no consensus on their existence and structure has been reached yet. One of the most widely debated questions is whether flow-induced precursors are crystalline or noncrystalline. A combination of wide- and small-angle X-ray scattering (WAXS and SAXS) is an effective technique to verify

the existence and probe the structure of precursors, as WAXS is sensitive to atomic order while SAXS probes density fluctuations in nanometer scale. Working on an in-house SAXS/WAXS setup with rotating anode as X-ray source, Katayama et al.⁴⁵ have already observed that density fluctuation appeared early than crystalline order in 1967. As the structure was obtained from a steady spinning line, it might be the first evidence for flow-induced noncrystalline precursors. With the development of the synchrotron radiation and detecting system, the appearance of SAXS signals like streaks from so-called shish structure earlier than that of crystalline signal from WAXS has been observed on samples after or during step shear at relatively high temperature by several groups.^{18,46–48} Combining with other results from spectroscopy like infrared and dielectric,^{49–51} optical microscopy,^{52–55} and computer simulation,^{56,57} flow-induced precursors can be either crystalline at low temperature or noncrystalline at high temperature, where the latter may be bundles with conformational ordered and oriented chain segments.⁵⁸ Based on their findings, molecular models have been proposed.^{58,59} In the theoretical models, it was proposed that precursors can be molecular clusters which transform into athermal nuclei and dormant

Received: March 13, 2014

Revised: May 16, 2014

Published: June 23, 2014

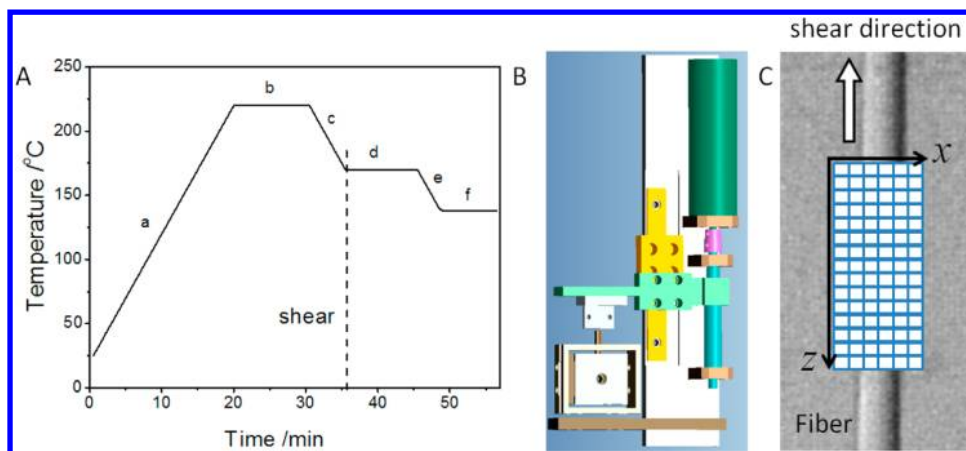


Figure 1. (A) Graphical representation of the testing protocol: the sandwiched iPP/fiber samples were (a) heated to 220 °C with a rate of 10 °C/min and (b) kept at 220 °C for 10 min to eliminate thermal history and then (c) cooled to T_s with a rate of 10 °C/min. (d) Immediately after cessation of shear at T_s , SR- μ SXRD was performed, which was about 10 min. After measurement at T_s , the samples were (e) cooled to 138 °C (f) for isothermal crystallization, during which SR- μ SXRD was applied to follow the structure evolution. (B) Schematic drawing of fiber pulling device. (C) Schematic diagram of fiber pulling and SR- μ SXR mapping path.

precursors which can be active or dormant according to their size. However, even with synchrotron radiation source, the difference of sensitivities of SAXS and WAXS is always a debating issue in the community, which may not resolve whether flow-induced precursors are crystalline or noncrystalline. Polec et al. reported the temperature dependence of inducing isotactic polypropylene (iPP) precursors from 150 to 170 °C, and the formation of crystalline and noncrystalline precursors is evidenced at 150 °C and above, respectively.⁴⁸ Zhao et al. studied shear-induced crystalline precursor of iPP at 148 °C.⁵⁴ Hsiao provided evidence of the oriented noncrystalline iPP precursors at 165 and 175 °C.^{28,60} Balzano et al. reported that with a high shear rate crystalline precursors of polyethylene can be produced around the equilibrium temperature.⁴⁶ Above studies show at temperatures near or around the melting point, flow-induced precursors still contain no or limited crystal. At temperatures higher than the melting point, it is more difficult to justify the structure of precursors; thus, techniques with higher detection sensitivity are required.

Because of high brilliant beam, synchrotron radiation scanning X-ray microdiffraction (SR- μ SXRD) is a highly sensitive detecting technique with high temporal and spatial resolution, which may benefit the understanding of flow-induced precursors. In addition to the intrinsic advantage due to the high brilliant beam, high temporal and spatial resolution of SR- μ SXRD can enhance the detecting sensitivity in two aspects. Flow-induced precursors are normally distributed inhomogeneously in space.⁶¹ Normal synchrotron radiation WAXS with large spot size may not be able to probe the weak signal from the small volume of precursors, as the signal is averaged over the whole large detection volume with only scattering from amorphous, while SR- μ SXRD is possible to detect the microdomain of precursors alone and prevent from spatially averaging, which can enhance the sensitivity dramatically. The time resolution of SR- μ SXRD is also beneficial to the sensitivity, as flow-induced precursors may be unstable and vanish over time.⁶² With those advantages, SR- μ SXRD has already been employed by some groups in the study on flow-induced precursors. The structure of shear-induced frozen precursors with shish-kebab morphology has been studied with SR- μ SXRD by Alfonso and co-workers.⁶³ They proposed that shish first formed from a few parallel chains

while lamellar assembly grew later simultaneously with the emergence of WAXS peaks. The experiment result suggests the formation of flow-induced noncrystalline precursors. With SR- μ SXRD, Kanaya et al.⁶⁴ showed that shear-induced precursors contained limited crystallinity with higher thermal stability than normal lamellar crystals. The above two SR- μ SXRD studies seem reaching contrary conclusion on the structure of precursors, which may be due to their different experimental procedures. Concerning experimental procedure, *in situ* time and spatial resolved SR- μ SXRD study on samples sheared at a wide temperature range may provide more evidence on the structure of precursors.

The present study investigates the nature and spatial distribution of flow-induced precursors over a broad temperature range with SR- μ SXRD. The method of pulling a single glass fiber through a thin polymer film is used to induce precursors, which is evidenced as an effective method to produce an intense and localized shear field.^{65–67} Our results show that the nature of flow-induced precursors is determined by the shear temperature, providing a high shear rate was introduced. At shear temperatures around or below the melting temperature, crystalline precursors can be induced, while at temperatures higher than the melting temperature but lower than the equilibrium melting temperature, noncrystalline precursors are generated.

EXPERIMENTAL SECTION

Material and Sample Preparation. The iPP used in this study was kindly supplied by SABIC-Europe. The melt flow index is about 0.3 g/10 min (230 °C/2.16 kg, ASTM D1238). Number-average molecular weight (M_n) and weight-average molecular weight (M_w) are 150 and 720 kg/mol, respectively. The melting temperature was found to be around 165 °C with a differential scanning calorimeter. The iPP films with thickness of ca. 50 μ m were prepared by compression molding. Glass fiber with diameter of ca. 15 μ m was embedded between two iPP films. The obtained sandwich was heated to 220 °C to erase thermal history under a nitrogen atmosphere. It worth pointing out that Monasse carried out the most similar work on a range of molecular weights of i-PP,^{65,66} the degree of growth rate at shear field is related to molecular weight, especially M_w . The shear efficiency is enhanced with high molecular weight distribution. The present sample has high M_w and molecular polydispersity of 4.8. It can be inferred that the fiber shear efficiency is pronounced.

In Situ SR- μ SXRD Measurement. The experimental protocol is shown in Figure 1A. The iPP/fiber samples, which were put between two Kapton films, were first heated up to 220 °C with a rate of 10 °C/min and kept for 10 min to erase thermal history. The fiber was pulled through the melt at a rate of 2 mm/s over a distance of 5 mm after cooling the sample to shear temperature (T_s). The shear rate $\dot{\gamma}$ at the interface is calculated according to the following equation proposed by Monasse⁶⁶

$$\dot{\gamma}(r) = \frac{1-n}{n} \frac{1}{r^{1/n}} \left[\frac{1}{r_f^{1-1/n} - r_e^{1-1/n}} \right] V_f$$

where r_e and r_f are the half-thickness of the polymer film and fiber radii, respectively. r is the location of the considered point in the polymer ($r_f \leq r \leq r_e$), and n is the exponent in the viscosity power law equation $\eta = K\dot{\gamma}^{n-1}$ with K the consistency. r_e and r_f are 50 and 10 μm , and V_f is 2000 $\mu\text{m/s}$. The values of n calculated from viscosity, which was obtained with small-amplitude oscillatory shear measurements, were 0.2 and 0.27 at 170 and 180 °C, respectively. The result indicates the shear rate is larger than 100 s^{-1} within the layer with thickness of 5 μm near the fiber surface.

Various T_s were carried out in this work, which were 160, 165, 170, 175, and 180 °C, and the corresponding samples were named as S_{160} , S_{165} , S_{170} , S_{175} , and S_{180} , respectively. Immediately after shear, the region around the fiber was scanned with SR- μ SXRD for about 10 min. Then the above samples were immediately cooled to 138 °C for isothermal crystallization. SR- μ SXRD was simultaneously employed to map the same sample area as did at T_s . For the convenience of description, these samples cooled to 138 °C were labeled as $S_{160-138}$, $S_{165-138}$, $S_{170-138}$, $S_{175-138}$, and $S_{180-138}$, where the first and second numbers in the subscript are the shear and crystallization temperatures, respectively.

The fiber pulling was applied with a homemade fiber pulling device coupled with a hot stage, which can be combined with SR- μ SXRD experiment stage. The pulling device can heat the samples from ambient temperature to 300 °C with a temperature uncertainty of ± 0.1 °C. The schematic drawing of fiber pulling device is shown in Figure 1B. During pulling, one end of the fiber was mounted on the clamp of the fiber pulling device, and the other end was embedded in the molten polymer film. The fiber was pulled in vertical direction as shown in Figure 1C. The SR- μ SXRD experiment was performed at the BL15U beamline in Shanghai Synchrotron Radiation Facility (SSRF). X-ray beam with a wavelength of 0.123 nm was used. The size of X-ray beam is $4.9 \times 5.3 \mu\text{m}^2$, which is determined with the beam profile. Diffraction patterns were collected with Mar165 CCD. During mapping, optical microscope (OM) images were first snapshoted by a CCD camera from the normal direction of the sample. Then it was switched to Mar165 CCD by motor for continuous SR- μ SXRD mapping measurement. The samples were first moved along the X-axis with a rate of 5 s/step, each step is equal to 7 μm , and 6 steps are needed in one row. Then the sample was moved to the second row and scanned with the same direction and velocity. Fifteen rows were scanned in total. As shown in Figure 1C, the scanned region near the fiber is $105 \times 42 \mu\text{m}^2$. Note that the scanned area for S_{170} is $70 \times 56 \mu\text{m}^2$, 10 rows were scanned, and every row possesses 8 steps. In addition to SR- μ SXRD measurements, the growth process of shear-induced crystal was also followed with optic microscopy (OM) (Olympus) separately.

The relative crystallinity X_c is calculated using the equation

$$X_c = \frac{A_c}{A_c + A_a} \times 100\%$$

where A_c and A_a are peak area of crystal diffraction peaks and amorphous peak, respectively. Here it should be noted the calculated crystallinity does not represent the crystallinity of crystals/precursor itself, since the X-ray signal inevitably includes the signal from the melt outside the crystals exposed to the X-ray and sometimes even contains the signal from the fiber, which will result in the low estimation of crystallinity.

RESULTS

In Situ OM Observation. The OM images of S_{160} immediately after shear as well as $S_{160-138}$ during isothermal crystallization are shown in Figure 2. As shown in the

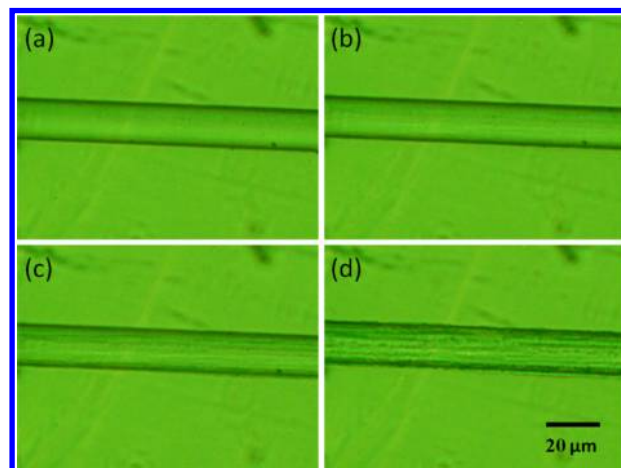


Figure 2. OM images of (a) S_{160} immediately after shear at 160 °C and $S_{160-138}$ crystallized for (b) 2, (c) 4, and (d) 6 min.

micrograph taken at 160 °C, no crystal can be seen on the fiber surface of S_{160} (see Figure 2a). However, after isothermal crystallization for 2 min, crystals are presented in a narrow region on the fiber surface in the microscopy image while no crystal formed beyond the fiber. The micrographs after crystallization for longer time show obvious crystals around the fiber surface. Since the fiber itself has no ability to induce nucleation,^{27,63} the preference of emergence and growth of crystal on the fiber surface is a clear evidence of the formation of flow-induced precursors, which may be due to residual perturbation around the fiber surface, though the precursors cannot be recognized by OM.

In Situ SR- μ SXRD Observation on Flow-Induced Precursors. *In situ* SR- μ SXRD measurements were performed to study the nature of flow-induced precursors immediately after cessation of shear at T_s , ranging from 160 to 180 °C. The diagrammatic figure of the mapping spots in Figure 3a shows SR- μ SXRD results on the iPP melt after shear at 160 °C. On the fiber surface, the crystalline signal can be viewed at all detected points. In the region 7 or 14 μm away from the fiber, the crystalline signal still can be observed, though the diffraction intensity decreases (see Figure 3b). In the region 21 μm or further away from the fiber, no crystalline signal appears. This indicates that the shear field is highly localized. With increasing the distance from the fiber, the intensity of shear field decreases drastically, so that crystal is hard to be induced. All diffraction signals are located in the equatorial direction and show narrow azimuthal width, indicating that crystal is highly orientated with molecular chains along the shear direction (see Figure 3b). The crystal signal is so weak that integration in full azimuthal angle range would blur the crystalline diffractions. Therefore, one-dimensional X-ray spectra were also obtained through integration within the narrow azimuthal width in the equatorial direction. Figure 3c shows all X-ray spectra in one row. Three sharp peaks located at 11.2°, 13.5°, and 14.8° appear in the X-ray spectrum, indicating the presence of α -form crystal. From the X-ray

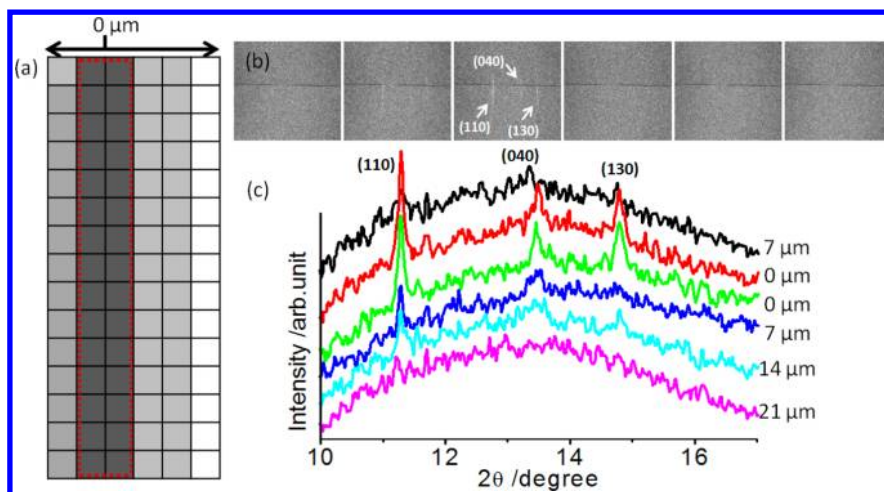


Figure 3. (a) Diagrammatic figure of the mapping spots on S₁₆₀; the gray and light gray spots represent strong and weak diffraction observed at the corresponding scanned spots, respectively, while the white ones indicate the absence of crystal. The darker color indicates higher crystallinity. The dashed line indicates the position of fiber. (b) SR-μSXR diffraction patterns of one row and (c) the corresponding X-ray spectra.

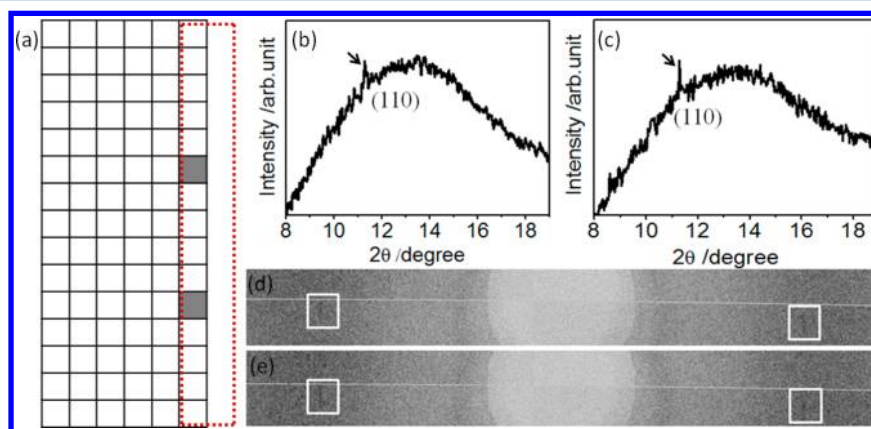


Figure 4. (a) Diagrammatic figure of the mapping spots on S₁₆₅; the gray spots indicate crystal diffraction observed at the corresponding scanned spots, while the white ones do not. The dashed line indicates the position of fiber. The 1D intensity profiles of the two crystalline SR-μSXR patterns are shown in (b) and (c), and the corresponding diffraction patterns are shown in (d) and (e), respectively.

spectra, the crystallinity at different detected points is also estimated. The highest crystallinity is around $0.29 \pm 0.03\%$.

The diagrammatic figure of the mapping spots in Figure 4a shows the mapping result of SR-μSXR on S₁₆₅. It can be seen that only 2 of 90 detected points show crystalline diffraction. The intensity profiles and the corresponding SR-μSXR patterns of those two points are shown in Figures 4b–e. Only (110) diffraction of α -form crystal can be distinguished in the equatorial direction with narrow azimuthal width. The crystallinities of iPP at these two locations were about $0.06 \pm 0.03\%$ and $0.07 \pm 0.03\%$, respectively. Evidently, increasing T_s leads to significant decrease of the density and crystallinity of crystalline precursors, indicating that the chance to induce crystalline precursors becomes less with elevated T_s . It should be noted that such low crystallinity cannot be detected by normal X-ray setup with large beam size, which normally detects crystal with crystallinity in the order of 1%. Thanks to the high brightness of third general synchrotron radiation and development of X-ray microanalysis technology, the detection sensitivity of X-ray is improved greatly.

SR-μSXR studies were also carried out on samples sheared at higher temperatures, i.e., 170, 175, and 180 °C, where no crystalline signal was found at all detected points near the fiber

in these samples. For conciseness, only the results of S₁₇₀ are presented. Figure 5 shows the diagrammatic figure of the mapping spots and the intensity profiles of SR-μSXR patterns on S₁₇₀. It is obvious that no crystal signal can be observed. Putting the above results together, it is evident that T_s affects the efficiency of fiber shear on inducing precursors. Crystalline precursors were induced on the fiber surface at 160 and 165 °C.

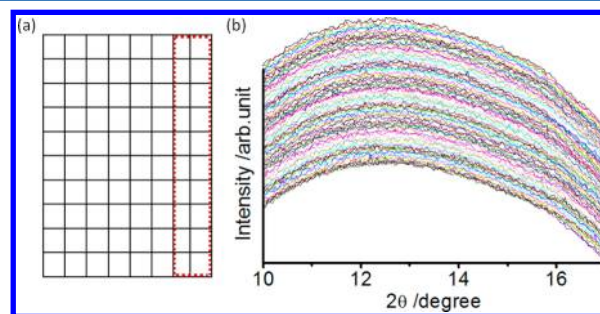


Figure 5. (a) Diagrammatic figure of the mapping spots on S₁₇₀; the white spots indicate that no crystal diffraction was observed. The dashed line indicates the position of fiber. The intensity profiles of SR-μSXR patterns are shown in (b).

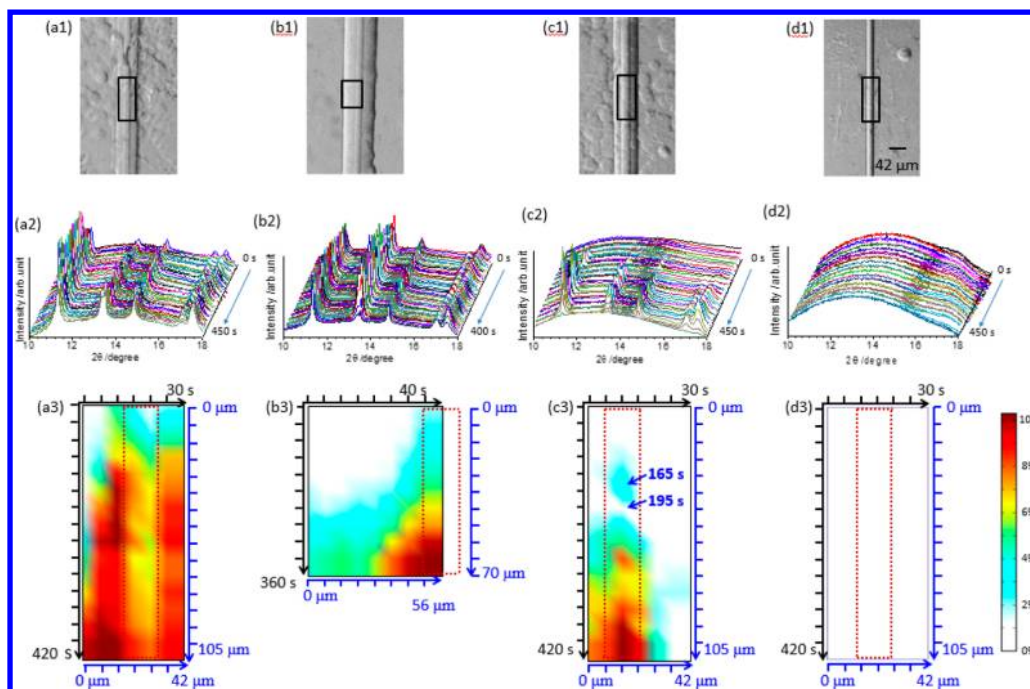


Figure 6. (a1–d1) Microscopy images after crystallization at 138 °C for about 10 min and (a2–d2) integrated 1D diffraction profiles integrated from the mapping diffraction patterns. (a3–d3) Distribution of crystallinity over time around the fiber surface (which is indicated in the microscopy images) during the second SR- μ SXRD mapping measurement of samples (a) $S_{160-138}$, (b) $S_{170-138}$, (c) $S_{175-138}$, and (d) $S_{180-138}$. The dashed line indicates the position of fiber.

The fiber surface of S_{160} is fully covered by α crystal, while for S_{165} crystals only appear at a few locations. When temperatures reached 170 °C or higher, no crystal was induced on the fiber surface.

Isothermal Crystallization at 138 °C (Samples Sheared at T_s). The above SR- μ SXRD study shows that crystalline precursors were induced by shear at temperatures of 160 and 165 °C, which confirms some early reports in this aspect. At 170, 175, and 180 °C no crystalline signal was observed; however, it is not sufficient to justify whether noncrystalline precursors are induced or not yet. In this section, this question is answered through their influence on subsequent isothermal crystallization at low temperature, as the presence of shear-induced precursors is expected to accelerate the crystallization process and lead to the formation of shish-kebab or row nuclei. SR- μ SXRD measurements on samples $S_{160-138}$, $S_{165-138}$, $S_{170-138}$, $S_{175-138}$, and $S_{180-138}$, which were cooled to 138 °C, were carried out to map the same region as did at T_s .

Before showing the SR- μ SXRD results, Figures 6a1–d1 first present the optic images of isothermally crystallized samples, which were taken after the completion of SR- μ SXRD mapping at 138 °C. As the crystallization behavior of $S_{165-138}$ was similar to that of $S_{170-138}$, the micrograph of isothermal crystallized on $S_{165-138}$ was not shown for conciseness. As shown in Figure 6, cylindrical crystal formed in all sheared samples except $S_{180-138}$. It has been reported that the fiber itself has no ability to induce crystallization at quiescent condition,^{27,63} which is also confirmed by the result of $S_{180-138}$. Even when spherulite forms far away from the fiber, no crystal appears on the fiber surface, which indicates that the fiber indeed cannot induce crystallization (see Figure 6d1). This also suggests that no precursor is induced at 180 °C, or they are not stable and vanish quickly even if precursors are induced at these temperatures. The appearance of cylindrical crystallites around

the fiber in $S_{160-138}$, $S_{170-138}$, and $S_{175-138}$ reflect the existence of shear-induced precursors at T_s . As revealed by SR- μ SXRD the precursors in S_{160} are crystalline, while the cylindrical crystallites in $S_{170-138}$ and $S_{175-138}$ are more possibly due to noncrystalline precursors induced by shear at T_s .

SR- μ SXRD were taken in the rectangular region indicated in the corresponding optic micrographs (Figure 6a1–d1). The integrated 1D diffraction profiles from mapping diffraction patterns are shown in Figure 6a2–d2. For conciseness, we present spatial distribution of crystallinity calculated from diffraction patterns directly, where a XZ coordinate is inserted to indicate the positions and arrows represent the scanning directions. Note that the scanning follows a row-by-row procedure and starts at the upper-left corner immediately after temperature reaching 138 °C. Hence, the SR- μ SXRD measurement is not only a spatial mapping but also a time-resolved study as crystallization evolves during scanning measurement. Following the time line, we established a XZ coordinate for time. It takes about 30 or 40 s to scan one row for different samples.

For the sample of $S_{160-138}$ (see Figure 6a3), crystals have already grown near the fiber surface at the beginning of isothermal crystallization, as crystals already formed at 160 °C after shear. Cooling down to 138 °C promotes fast growth without a nucleation process. The difference of crystallinity in one row is more related to the distance from fiber surface rather than time difference, as scanning one row takes rather short time (30 s). This difference reflects crystal growth in the radial direction away from fiber, as nucleation takes place near fiber surface. On the other hand, assuming that distribution of nuclei near fiber surface is homogeneous, the crystallinity in one column (Z-axis) reflects time evolution of crystallinity or crystallization kinetics. Indeed, crystallinity increases either with spatial axis from up to bottom or with time increase. Here note

that the lower crystallinity in the fiber interface than that outside is due to the influence of fiber on the calculation of the crystallinity. During the calculation of crystallinity the influence of fiber was not eliminated in the region near the fiber, which was assumed as amorphous, resulting in the lower calculated crystallinity. For $S_{170-138}$, only half of the fiber side is scanned. The crystal forms and grows in the beginning of the isothermal crystallization. As no crystalline precursor is observed after shear at 170 °C, this may be due to a fast transformation from noncrystalline precursors into crystalline nuclei during cooling or at 138 °C. Because the precursors form mainly at fiber/polymer interface and grows away from the fiber at the beginning of the isothermal crystallization, the crystallinity in the region near the fiber is slightly higher than the region away from the fiber. Nevertheless, due to lower nucleation density, the overall growth rate of $S_{170-138}$ is significantly slower than that of $S_{160-138}$. As shown in Figure 6b2, the 2D crystallinity distribution exhibits a damping and an increasing trends in X- and Z-axis directions, respectively, which represents an ongoing growth process. It needs to be noted that due to our operational error, only a partial area in the one side of the fiber was scanned. Different from $S_{160-138}$ and $S_{170-138}$, it takes an induction time of about 165 s for crystal signal to appear in $S_{175-138}$. The existence of induction period is consistent with the noncrystalline nature of precursors, which require time to transform into stable nuclei for further crystal growing. Note that for the spot with crystallization time of 195 s its crystallinity is lower than other areas, which could be due to heterogeneous distribution of precursors. Nevertheless, as shown in Figure 6c1, cylindrical crystallites form in all location near the fiber surface, providing crystallization time is long enough.

As Z-axis can be treated as a time axis, the crystallinity from the column near the fiber surface is used to represent nucleation and growth kinetics of crystals, which is summarized in Figure 7 for all samples. The time evolutions of crystallinity

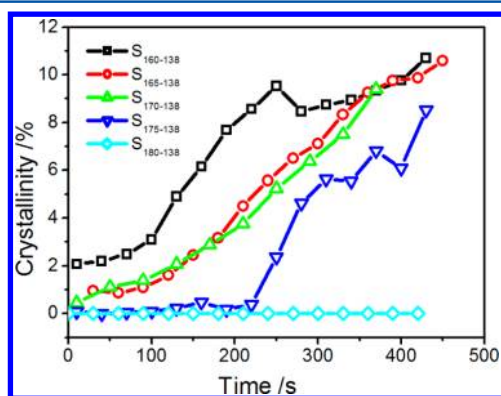


Figure 7. Evolution in crystallinity during isothermal crystallization at 138 °C along the Z-axis or said with time near the fiber surface after shear at different temperatures.

curves indicate that initial T_s affects the consequent crystallization kinetics. Higher T_s corresponds to slower crystallization rate, indicating either concentration or ordering of precursors decreases with the increase of temperature. This seems rather logical as the stability of precursors should decrease with the increase of temperature. The existence of an induction period for the sample sheared at temperature of 175 °C is further manifested in Figure 7, which supports that a

transition from initial noncrystalline precursors to nuclei is required. On the other hand, the induction time for the transformation from noncrystalline precursors to nuclei of $S_{175-138}$ is much shorter than that of $S_{180-138}$, confirming the presence of noncrystalline precursors in the former sample. No crystallization occurs during measurement time of 450 s from $S_{180-138}$.

From above results, it can be seen that below or around 165 °C crystalline precursors can be formed; above 165 °C but lower than 180 °C, noncrystalline precursor can be formed; above or around 180 °C, no precursor was formed. Note that 180 °C was close to the equilibrium melting point, while it was reported that 186 °C is the equilibrium melting point.^{68,69} Thus, it can be concluded that noncrystalline precursors could be generated by high shear rate between the melting point and the equilibrium melting temperatures.

Not only the crystallization kinetics but also the orientation parameters reduce with increasing T_s . Figure 8 shows the

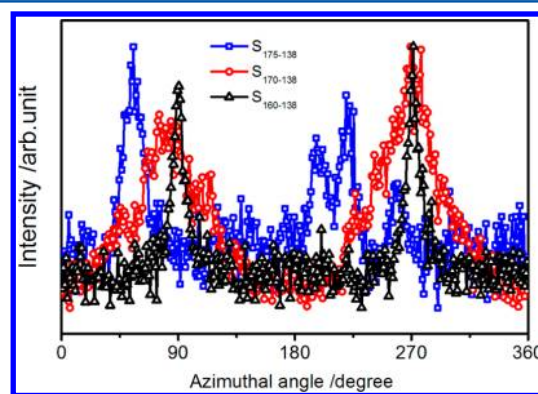


Figure 8. One-dimensional azimuthal intensity curves of (040) plane of crystal on the fiber surface of $S_{160-138}$, $S_{170-138}$, and $S_{175-138}$.

intensity distribution of (040) peak along the azimuthal angle of crystal at the fiber/polymer interface on samples $S_{160-138}$, $S_{170-138}$, and $S_{175-138}$. The orientation of crystal decreases either with the distance away from the fiber surface on the same sample since the shear rate decays exponentially. Here only the orientation of crystal at the fiber surface was shown to obtain the temperature effect on orientation of crystals. Note that the starting point of azimuthal intensity integration is the meridional direction. The (040) diffraction of $S_{160-138}$ shows peaks at azimuthal angle of 90° and 270°, indicating that the polymer chains in the crystal are oriented along shear direction. Based on the full width at half-maximum (fwhm) of (040) diffraction, the orientation parameter is calculated to be about 0.97. For $S_{170-138}$ the (040) diffraction shows two wide peaks at 90° and 270° which exhibit a broader azimuthal width. The orientation parameter is about 0.35, which illustrates that the orientation of crystal induced by noncrystalline precursors is much lower than that induced by crystalline precursors. This may be due to the influence of relaxation at high temperature. The orientation of samples sheared at high temperatures is not as high as that of the samples sheared at low temperatures. Taking the $S_{175-138}$ as the example, the (040) diffraction of crystal at T_c shows peaks at 53°, 238°, 260°, and 299°, indicating that the crystal is not parallel to the flow direction strictly.

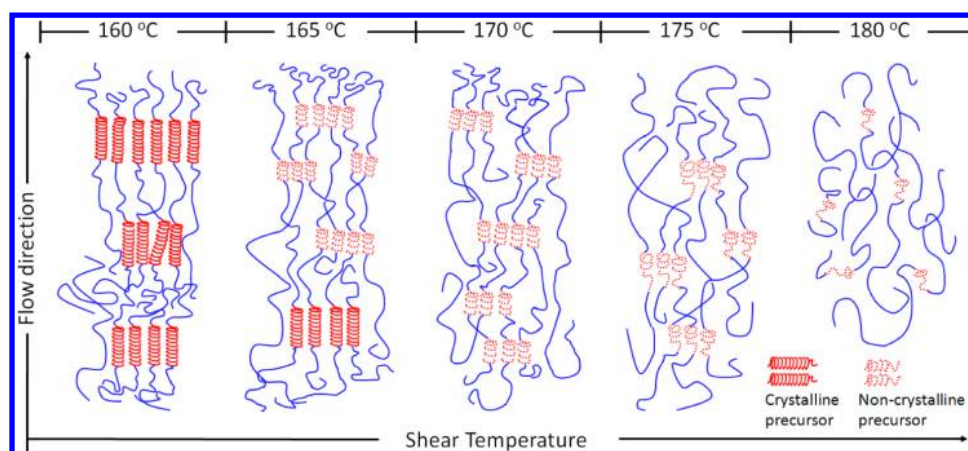


Figure 9. Schematic diagram of shear-induced precursors at various shear temperatures.

DISCUSSION

The above experiment results show that the most important factor determining the nature of flow-induced precursors is the T_s , providing a high shear rate are imposed. When T_s is around or below melting temperature, crystalline precursors are induced. With T_s between the melting point and the equilibrium melting temperatures, noncrystalline precursors could be generated by flow. Above equilibrium melting temperature, no precursor can be formed.

The existence of shear-induced crystalline precursors has been widely confirmed, which can be essentially treated as standard nucleation process under a nonequilibrium condition. Thus, here we focus our discussion on the noncrystalline precursors. Taking the results from S_{175} as the best example, three evidence support that noncrystalline precursors are induced by shear. (i) The formation of cylindrical crystallites in $S_{175-138}$ indicates that shear indeed induced some ordered structures at 175 °C. Starting from the cessation of fiber shear, it takes more than 10 min to complete SR- μ SXRD measurement at 175 °C and cooling process to 138 °C, which is far longer than the terminal relaxation time τ_d of iPP chains. The τ_d is 0.96 s at 160 °C and 0.65 s at 175 °C. This indicates the induced ordered structure is not simply chain orientation, which should be precursors involving multichain interaction with longer lifetime than the terminal time τ_d . (ii) The absence of any crystalline diffraction signal from S_{175} suggests that the precursors are noncrystalline. SR- μ SXRD has much higher detection sensitivity than in-house and normal synchrotron radiation X-ray setups. As mentioned above, the detection sensitivity of SR- μ SXRD reaches the order of 0.1%. With higher detection sensitivity of SR- μ SXRD, no crystal was observed from S_{175} . Nevertheless, as detection sensitivity is a never-ending debating issue, one can always argue the presence of tiny crystals lower than the detection sensitivity. For this concern, a third evidence is put forward: (iii) An induction time exists for $S_{175-138}$. If the crystalline nucleus is induced by shear at 175 °C, crystal should grow straightforwardly without induction time like S_{160} and S_{165} when samples were cooled down to 138 °C. The induction time is the time for the transformation of noncrystalline precursors into crystalline nuclei. With this evidence, it can be safe to conclude that noncrystalline precursors are indeed induced by shear.

Based on above findings, flow-induced precursors at different T_s are schematically presented in Figure 9. In the polymer melt, polymer chains mainly exist in the form of random coil, and

shear induces the transition from coil to helix.^{70,71} Some parallelly arranged helices may form aggregates under the intermolecular force, which have relatively high thermal stability and thus can exist in the melt. At 160 °C, the aggregates of oriented chain segments can further develop into crystalline precursors, leading to the emergence of crystalline diffraction. While for 165 °C, only a tiny part of aggregates of oriented polymer chains can grow into crystalline precursors, other aggregates keep in the noncrystalline state. Thus, the precursors induced at this temperature contain both crystalline and noncrystalline ones. It was also reported by other groups that the noncrystalline precursors were metastable,⁷² and it may have fibrillar morphology which has higher density than normal melt.⁴⁷ At 170 °C, only noncrystalline precursors can be induced, and it can transform into crystalline nuclei quickly when temperature is cooling down. At 175 °C, noncrystalline precursors form and keep the freedom degree along the shear direction. The helices in the aggregates may be shorter; thus, an induction time is required during the crystallization process. When further increasing the T_s to 180 °C, shear-induced helices may relax back to random coils due to thermal fluctuation though some short helices exist in the melt; thus no precursors are observed.

CONCLUSION

In conclusion, *in situ* time and spatial resolved SR- μ SXRD was performed to investigate the existence and nature of flow-induced precursors over a broad temperature range. Shear temperature dependence of precursors' structure is suggested by experimental results, providing a high shear rate is imposed. Crystalline precursors were observed immediately after the cessation of shear with shear temperatures around or below the melting temperature. While in between melting and equilibrium melting temperatures, the absence of crystal diffraction at T_s and formation of cylindrical crystallites on the fiber surface after cooling suggest the generation of noncrystalline precursors, which are rather stable at shear temperature within SR- μ SXRD measurement time. Induction time necessary for the transformation from precursors to nuclei further indicates the disorder nature of noncrystalline precursors, the structure of which could be bundles of oriented and parallel arranged chain segments. Our study demonstrates the sensitivity of precursors' structure of shear temperatures, which will contribute to a clear and comprehensive picture of the flow-induced precursors and

help to settle the dispute on the nature of flow-induced precursors.

AUTHOR INFORMATION

Corresponding Authors

*E-mail: lixy81@ustc.edu.cn (X.L.).

*E-mail lbli@ustc.edu.cn (L.L.).

Notes

The authors declare no competing financial interest.

ACKNOWLEDGMENTS

This work is supported by the National Natural Science Foundation of China (51033004, 51120135002, 51227801, 51303166, and 51325301), the 973 program of MOST (2010CB934504), and “the Fundamental Research Funds for the Central Universities”. The experiment is carried out in the National Synchrotron Radiation Lab (NSRL) and Shanghai Synchrotron Radiation Facility (SSRF). The authors thank Dr. Ningdong Huang for assistance with English corrections and Sabic-Europe for providing iPP material.

REFERENCES

- (1) Kumaraswamy, G.; Issaian, A. M.; Kornfield, J. A. *Macromolecules* **1999**, *32* (22), 7537–7547.
- (2) Kumaraswamy, G.; Kornfield, J. A.; Yeh, F. J.; Hsiao, B. S. *Macromolecules* **2002**, *35* (5), 1762–1769.
- (3) Samon, J. M.; Schultz, J. M.; Hsiao, B. S. *Macromolecules* **2001**, *34* (6), 2008–2011.
- (4) Ward, I. M. *Makromol. Chem., Macromol. Symp.* **1988**, *22*, 59–82.
- (5) Perepelk, Ke. *Angew. Makromol. Chem.* **1972**, *22* (Mar 30), 181.
- (6) Janeschitzkriegl, H.; Eder, G.; Krobath, G.; Liedauer, S. *J. Non-Newtonian Fluid Mech.* **1987**, *23*, 107–122.
- (7) Yang, H. R.; Lei, J.; Li, L. B.; Fu, Q.; Li, Z. M. *Macromolecules* **2012**, *45* (16), 6600–6610.
- (8) Bashir, Z.; Hill, M. J.; Keller, A. J. *Mater. Sci. Lett.* **1986**, *5* (9), 876–878.
- (9) Li, L. B.; de Jeu, W. H. *Interphases Mesophases Polym. Cryst. II* **2005**, *181*, 75–120.
- (10) Housmans, J. W.; Steenbakkers, R. J. A.; Roozmond, P. C.; Peters, G. W. M.; Meijer, H. E. H. *Macromolecules* **2009**, *42* (15), 5728–5740.
- (11) Somani, R. H.; Hsiao, B. S.; Nogales, A.; Srinivas, S.; Tsou, A. H.; Sics, I.; Balta-Calleja, F. J.; Ezquerro, T. A. *Macromolecules* **2000**, *33* (25), 9385–9394.
- (12) Seki, M.; Thurman, D. W.; Oberhauser, J. P.; Kornfield, J. A. *Macromolecules* **2002**, *35* (7), 2583–2594.
- (13) Hobbs, J. K.; Humphris, A. D. L.; Miles, M. J. *Macromolecules* **2001**, *34* (16), 5508–5519.
- (14) Sakellarides, S. L.; Mchugh, A. J. *Rheol. Acta* **1987**, *26* (1), 64–77.
- (15) Keller, A.; Kolnaar, H. W. H. In *Processing of Polymers*; Meijer, H. E. H., Ed.; VCH: New York, 1997; Vol. 18, p 189.
- (16) Bassett, D. C.; Frank, F. C.; Keller, A. *Nature* **1959**, *184* (4689), 810–811.
- (17) Murase, H.; Ohta, Y.; Hashimoto, T. *Macromolecules* **2011**, *44* (18), 7335–7350.
- (18) Kimata, S.; Sakurai, T.; Nozue, Y.; Kasahara, T.; Yamaguchi, N.; Karino, T.; Shibayama, M.; Kornfield, J. A. *Science* **2007**, *316* (5827), 1014–1017.
- (19) Kanaya, T.; Takayama, Y.; Ogino, Y.; Matsuba, G.; Nishida, K. *Lect. Notes Phys.* **2007**, *714*, 87–96.
- (20) Janeschitz-Kriegl, H.; Eder, G. *J. Macromol. Sci., Part B: Phys.* **2007**, *46* (3), 591–601.
- (21) Somani, R. H.; Yang, L.; Zhu, L.; Hsiao, B. S. *Polymer* **2005**, *46* (20), 8587–8623.
- (22) Yamazaki, S.; Hikosaka, M.; Toda, A.; Wataoka, I.; Gu, F. M. *Polymer* **2002**, *43* (24), 6585–6593.
- (23) Shen, B.; Liang, Y. R.; Kornfield, J. A.; Han, C. C. *Macromolecules* **2013**, *46* (4), 1528–1542.
- (24) Dukovski, I.; Muthukumar, M. J. *Chem. Phys.* **2003**, *118* (14), 6648–6655.
- (25) Shen, B.; Liang, Y. R.; Zhang, C. G.; Han, C. C. *Macromolecules* **2011**, *44* (17), 6919–6927.
- (26) Ezquerro, T. A.; LopezCabarcos, E.; Hsiao, B. S.; BaltaCalleja, F. J. *Phys. Rev. E* **1996**, *54* (1), 989–992.
- (27) Azzurri, F.; Alfonso, G. C. *Macromolecules* **2005**, *38* (5), 1723–1728.
- (28) Somani, R. H.; Yang, L.; Hsiao, B. S.; Agarwal, P. K.; Fruitwala, H. A.; Tsou, A. H. *Macromolecules* **2002**, *35* (24), 9096–9104.
- (29) Yang, L.; Somani, R. H.; Sics, I.; Hsiao, B. S.; Kolb, R.; Lohse, D. *J. Phys.: Condens. Matter* **2006**, *18* (36), S2421–S2436.
- (30) Ma, Z.; Balzano, L.; van Erp, T.; Portale, G.; Peters, G. W. M. *Macromolecules* **2013**, *46* (23), 9249–9258.
- (31) Ma, Z.; Balzano, L.; Peters, G. W. M. *Macromolecules* **2012**, *45* (10), 4216–4224.
- (32) Graham, R. S.; Olmsted, P. D. *Phys. Rev. Lett.* **2009**, *103* (11), 115702.
- (33) Okura, M.; Mykhaylyk, O. O.; Ryan, A. J. *Phys. Rev. Lett.* **2013**, *110* (8), 087801.
- (34) Balzano, L.; Rastogi, S.; Peters, G. *Macromolecules* **2011**, *44* (8), 2926–2933.
- (35) Mykhaylyk, O. O.; Fernyhough, C. M.; Okura, M.; Fairclough, J. P. A.; Ryan, A. J.; Graham, R. *Eur. Polym. J.* **2011**, *47* (4), 447–464.
- (36) Cui, K. P.; Meng, L. P.; Tian, N.; Zhou, W. Q.; Liu, Y. P.; Wang, Z.; He, J.; Li, L. B. *Macromolecules* **2012**, *45* (13), 5477–5486.
- (37) Cui, K.; Meng, L.; Ji, Y.; Li, J.; Zhu, S.; Li, X.; Tian, N.; Liu, D.; Li, L. *Macromolecules* **2014**, *47* (2), 677–686.
- (38) Mykhaylyk, O. O.; Chambon, P.; Graham, R. S.; Fairclough, J. P. A.; Olmsted, P. D.; Ryan, A. J. *Macromolecules* **2008**, *41* (6), 1901–1904.
- (39) Ogino, Y.; Fukushima, H.; Takahashi, N.; Matsuba, G.; Nishida, K.; Kanaya, T. *Macromolecules* **2006**, *39* (22), 7617–7625.
- (40) Yang, L.; Somani, R. H.; Sics, I.; Hsiao, B. S.; Kolb, R.; Fruitwala, H.; Ong, C. *Macromolecules* **2004**, *37* (13), 4845–4859.
- (41) Kanaya, T.; Matsuba, G.; Ogino, Y.; Nishida, K.; Shimizu, H. M.; Shinohara, T.; Oku, T.; Suzuki, J.; Otomo, T. *Macromolecules* **2007**, *40* (10), 3650–3654.
- (42) Matsuba, G.; Sakamoto, S.; Ogino, Y.; Nishida, K.; Kanaya, T. *Macromolecules* **2007**, *40* (20), 7270–7275.
- (43) Elmoumni, A.; Gonzalez-Ruiz, R. A.; Coughlin, E. B.; Winter, H. H. *Macromol. Chem. Phys.* **2005**, *206* (1), 125–134.
- (44) Hashimoto, T.; Murase, H.; Ohta, Y. *Macromolecules* **2010**, *43* (16), 6542–6548.
- (45) Katayama, K.; Amano, T.; Nakamura, K. *Kolloid Z. Z. Polym.* **1968**, *226* (2), 125.
- (46) Balzano, L.; Kukalyekar, N.; Rastogi, S.; Peters, G. W. M.; Chadwick, J. C. *Phys. Rev. Lett.* **2008**, *100* (4), 048302.
- (47) Hsiao, B. S.; Yang, L.; Somani, R. H.; Avila-Orta, C. A.; Zhu, L. *Phys. Rev. Lett.* **2005**, *94* (11), 117802.
- (48) Polec, I. A.; Fujiwara, T.; Kanaya, T.; Deng, C. *Polymer* **2012**, *53* (16), 3540–3547.
- (49) An, H. N.; Zhao, B. J.; Ma, Z.; Shao, C. G.; Wang, X.; Fang, Y. P.; Li, L. B.; Li, Z. M. *Macromolecules* **2007**, *40* (14), 4740–4743.
- (50) Geng, Y.; Wang, G. L.; Cong, Y. H.; Bai, L. G.; Li, L. B.; Yang, C. L. *Macromolecules* **2009**, *42* (13), 4751–4757.
- (51) Soccio, M.; Nogales, A.; Lotti, N.; Munari, A.; Ezquerro, T. A. *Phys. Rev. Lett.* **2007**, *98* (3), 037801.
- (52) Hayashi, Y.; Matsuba, G.; Zhao, Y. F.; Nishida, K.; Kanaya, T. *Polymer* **2009**, *50* (9), 2095–2103.
- (53) Matsuba, G.; Zhao, Y. F.; Teratani, M.; Hayashi, Y.; Takayama, Y.; Ogino, Y.; Nishida, K.; Kanaya, T. *Kobunshi Ronbunshu* **2009**, *66* (10), 419–427.
- (54) Zhao, Y.; Hayasaka, K.; Matsuba, G.; Ito, H. *Macromolecules* **2013**, *46* (1), 172–178.

- (55) Zhao, Y. F.; Matsuba, G.; Moriwaki, T.; Ikemoto, Y.; Ito, H. *Polymer* **2012**, *53* (21), 4855–4860.
- (56) Hu, W. B.; Frenkel, D.; Mathot, V. B. F. *Macromolecules* **2002**, *35* (19), 7172–7174.
- (57) Wang, M. X.; Hu, W. B.; Ma, Y.; Ma, Y. Q. *Macromolecules* **2005**, *38* (7), 2806–2812.
- (58) Ziabicki, A.; Alfonso, G. C. *Macromol. Symp.* **2002**, *185*, 211–231.
- (59) Roozmond, P. C.; Steenbakkers, R. J. A.; Peters, G. W. M. *Macromol. Theory Simul.* **2011**, *20* (2), 93–109.
- (60) Somani, R. H.; Yang, L.; Hsiao, B. S. *Physica A* **2002**, *304* (1–2), 145–157.
- (61) Wang, Z. G.; Hsiao, B. S.; Sirota, E. B.; Agarwal, P.; Srinivas, S. *Macromolecules* **2000**, *33* (3), 978–989.
- (62) Jiang, X.; Liao, Q.; Zhou, J. J.; Wang, Z. H.; Chan, C. M.; Li, L. J. *Polym. Sci., Part B: Polym. Phys.* **2013**, *51* (11), 907–914.
- (63) Gutierrez, M. C. G.; Alfonso, G. C.; Riekel, C.; Azzurri, F. *Macromolecules* **2004**, *37* (2), 478–485.
- (64) Kanaya, T.; Polec, I. A.; Fujiwara, T.; Inoue, R.; Nishida, K.; Matsuura, T.; Ogawa, H.; Ohta, N. *Macromolecules* **2013**, *46* (8), 3031–3036.
- (65) Monasse, B. J. *Mater. Sci.* **1992**, *27* (22), 6047–6052.
- (66) Duplay, C.; Monasse, B.; Haudin, J. M.; Costa, J. L. *J. Mater. Sci.* **2000**, *35* (24), 6093–6103.
- (67) Jay, F.; Haudin, J. M.; Monasse, B. J. *Mater. Sci.* **1999**, *34* (9), 2089–2102.
- (68) Mezghani, K.; Campbell, R. A.; Phillips, P. J. *Macromolecules* **1994**, *27* (4), 997–1002.
- (69) Bond, E. B.; Spruiell, J. E. *J. Appl. Polym. Sci.* **2001**, *81* (1), 229–236.
- (70) Geng, Y.; Wang, G. L.; Cong, Y. H.; Bai, L. G.; Li, L. B.; Yang, C. L. *J. Polym. Sci., Part B: Polym. Phys.* **2010**, *48* (2), 106–112.
- (71) An, H. N.; Li, X. Y.; Geng, Y.; Wang, Y. L.; Wang, X.; Li, L. B.; Li, Z. M.; Yang, C. L. *J. Phys. Chem. B* **2008**, *112* (39), 12256–12262.
- (72) Cavallo, D.; Azzurri, F.; Balzano, L.; Funari, S. S.; Alfonso, G. C. *Macromolecules* **2010**, *43* (22), 9394–9400.